Inorganic Chemistry

Article

pubs.acs.org/IC

*B*1-to-*B*2 Structural Transitions in Rock Salt Intergrowth Structures

Takafumi Yamamoto,[†] Yoji Kobayashi,[†] Taku Okada,[‡] Takehiko Yagi,[‡] Takateru Kawakami,[§] Cédric Tassel,[†] Shota Kawasaki,[†] Naoyuki Abe,[†] Ken Niwa,[∥] Takumi Kikegawa,[⊥] Naohisa Hirao,[#] Mikio Takano,[▽] and Hiroshi Kageyama*[,†,▽]

[†]Department of Energy and Hydrocarbon Chemistry, Graduate School of Engineering, Kyoto University, Nishikyo, Kyoto 615-8510, Japan

[‡]Research Institute for Solid State Physics, University of Tokyo, 5-1-5 Kashiwanoha, Kashiwa, Chiba 277-8581, Japan

[§]Institute of Quantum Science, Nihon University, Chiyoda, Tokyo 101-8308, Japan

[∥]Department of Materials Science and Engineering, Nagoya University, Nagoya, Aichi 464-8603, Japan

[⊥]Photon Factory, Institute of Material Structure Science, High Energy Acceleration Research Organization (KEK), 1-1 Oho, Tsukuba, Ibaraki 305-0801, Japan

[#]Japan Synchrotron Radiation Research Institute, Hyogo 679-5198, Japan

[▽]Institute for Integrated Cell-Material Sciences, Kyoto University, Sakyo, Kyoto 606-8501, Japan

Supporting Information

ABSTRACT: The rock salt (*B*1) structure of binary oxides or chalcogenides transforms to the CsCl (*B*2) structure under high pressure, with critical pressures P_s depending on the cation to anion size ratio (R_c/R_a). We investigated structural changes of A_2MO_3 (A = Sr, Ca; M = Cu, Pd) comprising alternate 7-fold *B*1 AO blocks and corner-shared MO_2 square-planar chains under pressure. All of the examined compounds exhibit a structural transition at P_s = 29−41 GPa involving a change in the A-site geometry to an 8-fold *B*2 coordination. This observation demonstrates, together with the high pressure study on the structurally related $Sr_3Fe_2O_5$, that the *B*1-to-*B*2 transition generally occurs in these intergrowth structures. An empirical relation of P_s and the R_c/R_a ratio for the binary system holds well for the intergrowth structure also, which means that P_s is predominantly determined by the rock salt blocks. However, a large deviation from the relation is found in $LaSrNiO_{3.4}$, where oxygen atoms partially occupy the apical site of the MO_4 square plane. We predict furthermore the occurrence of the same structural transition for Ruddlesden−Popper-type layered perovskite oxides $(AO)(AMO_3)_n$, under higher pressures. For investigating the effect on the physical properties, an electrical resistivity of Sr_2CuO_3 is studied.

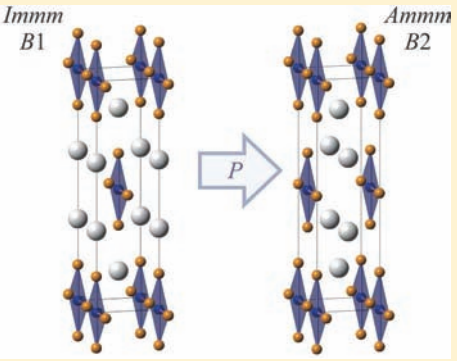

1. INTRODUCTION

Crystal structures of minerals under high pressure have long been of great interest in structural chemistry and geology. For example, silica SiO_2 has various polymorphs depending on temperature and pressure.[1−4] The recent discovery of postperovskite structure in $MgSiO_3$ may account for the D″ seismic discontinuity.[5] Among a numerous number of pressure-induced structural transitions, the transition from *B*1(NaCl) to *B*2(CsCl) is perhaps the most systematically studied system and best understood from both experimental and theoretical points of view. This is because both *B*1 and *B*2 structures are simple ionic structures, and MgO is believed to exhibit this transition in the Earth's lower mantle. So far, many ionic binary compounds AX (A = Ca, Sr, Ba: X = O, S, Se, Te) with the *B*1-type structure at ambient pressure are known to or are predicted to transform to the *B*2-type structure at high pressure.[6−18] It was furthermore revealed that, for a given X, the logarithm of transition pressure P_s shows a linear dependence on the ratio of the cation/anion radius, R_A/R_X (see Figure 1S in the Supporting Information).[6−8]

Pressure-induced magnetic/transport transitions have been recently observed at P_c = 33 GPa in the infinite layer structure $SrFeO_2$, that is, a spin-state transition (from high-spin state to intermediate-spin state), an insulator-to-metal transition, and an antiferromagnetic-to-ferromagnetic transition.[19] The two-legged spin ladder structure $Sr_3Fe_2O_5$, an intergrowth compound composed of alternate stacking of the SrO rock salt block and the $(SrFeO_2)_2$ ladder block along the *c* axis, also undergoes these three transitions at the nearly same pressure of P_c = 34 GPa.[20] Unexpectedly, the latter compound shows an additional structural transition from *Immm* to *Ammm* at P_s = 30 GPa.[20] The structural transition is of the first order and is characterized by the phase shift of the neighboring ladder blocks from (1/2,1/2,1/2) to (0,1/2,1/2). With this phase shift

Received: August 31, 2011
Published: October 21, 2011

of the ladder block, the coordination geometry around strontium changes from the 7-fold rock salt arrangement to the 8-fold CsCl arrangement. Therefore, this structural transition can be characterized as a *B*1-to-*B*2 transition within an intergrowth compound.

However, whether or not the *B*1-to-*B*2 transition is universal to structurally related intergrowth compounds is uncertain. Several considerations show that one cannot easily preclude the scenario that the FeO_4 square planes (or the ladder subunit in $Sr_3Fe_2O_5$) take a leading role in the structural transition. A series of *n*-legged spin ladder $Sr_{n-1}Cu_nO_{2n-1}$ (n = 2, 3, etc.),[21,22] obtained by high pressure synthesis, can be viewed as "quasi" infinite layer structures composed of the $(Cu_nO_{2n-1})^{2(n-1)-}$ layers intervened by $(n-1)Sr^{2+}$. Notice that the high pressure form of $Sr_3Fe_2O_5$ also forms the "quasi" infinite layer structure composed of $(Fe_2O_5)^{6-}$ layers intervened by $3Sr^{2+}$. Furthermore, the preservation of the piled ladders upon transition may be ascribed to Fe−Fe interactions between face-to-face FeO_4 square planes (i.e., metal−metal bonding), which are experimentally and theoretically shown to be strong.[23−26] The metal−metal bonding would become stronger under high pressure. Another source of complication is the proximity of P_s and P_c: the structural transition might be driven by certain interplay between energetically close states (S = 2 antiferromagnetic insulator vs S = 1 ferromagnetic metal).

In this study, we investigated the presence of pressure-induced structural transitions in one-dimensional (1D) compounds A_2MO_3 (A = Sr, Ca; M = Cu, Pd).[27,28] The crystal structure is shown in Figure 1a. A_2MO_3 is an intergrowth structure of the AO rock salt blocks and the 1D chains of corner-shared MO_2 squares (or one-legged ladders) and adopts the *Immm* space group. In $A_2Cu(II)O_3$, only the 3d x^2-y^2 orbital is active, and the metal−metal bonding between face-to-face CuO_4 square planes is negligibly small, in contrast with the case of $Sr_3Fe_2O_5$. All examined A_2MO_3 compounds exhibit the same type of structural transitions as $Sr_3Fe_2O_5$, which provides a unique opportunity to discuss the intrinsic nature of this transition and quantitative comparison with the well-studied binary systems. In addition, the effect of the partial oxygen filling at the apical vacant site was investigated through $LaSrNiO_{3.4}$. The electrical properties of Sr_2CuO_3 between the low- and high-pressure phases are compared in order to investigate the effect on the physical properties.

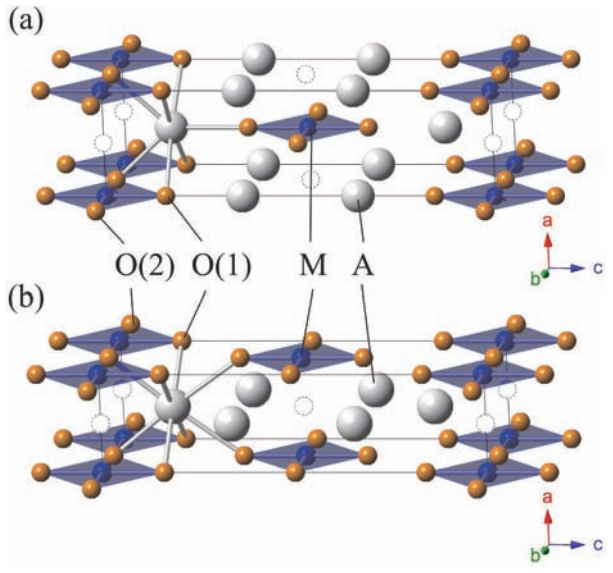

Figure 1. The A_2MO_3 structures (a) at low pressure ($P < P_s$) and (b) at high pressure ($P_s < P$). White, blue, and orange spheres represent A, M, and O atoms, respectively. Dotted circles represent apical vacant oxygen sites.

2. EXPERIMENTAL SECTION

Powder samples of Sr_2CuO_3, Ca_2CuO_3, and Sr_2PdO_3 were synthesized by the high-temperature ceramic method.[27,28] Stoichiometric amounts of $SrCO_3$ (99.99%), $CaCO_3$ (99.99%), CuO (99.99%), and PdO (99.99%) were mixed, pelletized, and fired at 1173 K for 24 h. Subsequently, the pellets were ground, repelletized, and heated at 1223 K for 24 h. The sample purities were checked with X-ray diffraction (XRD) measurement using a D8 ADVANCE diffractometer (BRUKER) equipped with a graphite monochromator and Cu Kα1 radiation (λ = 1.54056 Å). As shown in Figure 2S in the Supporting Information, all of the diffraction patterns were represented by the *Immm* space group, consistent with previous reports.[27,28] No impurity peaks were detected.

A powder sample of $LaSrNiO_{3.4}$ was synthesized topochemically by reducing a single-layered Ruddlesden−Popper type perovskite $LaSrNiO_4$. The $LaSrNiO_4$ precursor was prepared using a high temperature ceramic method from $SrCO_3$ (99.99%), predried La_2O_3 (99.99%), and NiO (99.99%). A pelletized stoichiometric mixture was heated at 1373 K in the air for 24 h, and at 1673 K in O_2 flowing for 48 h after an intermediate grinding. For reduction, $LaSrNiO_4$ and a 2 M excess of CaH_2 were finely ground in a N_2-filled glovebox, sealed in an evacuated Pyrex tube, and heated at 623 K for 24 h. Residual CaH_2 and CaO byproducts were removed from the final reaction phase by washing them with a 0.05 mol/L NH_4Cl/methanol solution. The tetragonal and orthorhombic lattice parameters of the precursor and the reduced phases are, respectively, a = 3.82699(5) Å and c = 12.4569(2) Å and a = 3.6856(3) Å, b = 3.8670(3) Å, and c = 12.708(1) Å. The oxygen amount in the reduced material was examined by thermogravimetric (TG) measurement using a TG-DTA 2000S (Bruker AXS). A 50.8 mg sample was put in a Pt pan, and α-Al_2O_3 was used as a reference. The measurements were performed by heating the sample at 10 K/min under a flow of oxygen with a flow rate of 100 mL/min. Figures 3S and 4S in the Supporting Information demonstrate that the composition is $LaSrNiO_{3.4}$. This stoichiometry is supported by the dependence of the lattice parameters on the oxygen content as reported in the literature for $LaSrNiO_{4-x}$, which was obtained by H_2 gas reduction from $LaSrNiO_4$.[29]

The laboratory XRD profiles under high pressures were recorded up to 43 GPa for Sr_2CuO_3, 54 GPa for Ca_2CuO_3, and 36 GPa for Sr_2PdO_3 using Mo Kα1 radiation from a 5.4 kW Rigaku rotating anode generator equipped with a 100 μm collimator. Powder samples were loaded into a 180 μm hole of preindented rhenium gaskets of the diamond-anvil cells (DAC). Helium was used as a pressure transmitting medium for Sr_2CuO_3, while a 4:1 methanol/ethanol mixture was used for Ca_2CuO_3 and Sr_2PdO_3. The fluorescence shift of ruby was used to calibrate the pressure. To estimate the pressure distribution along the sample, several ruby chips were placed inside the hole at different distances from its center. It was found that the pressure gradient at the samples increases with pressure but would not exceed 1 GPa for Sr_2CuO_3 and 4 GPa for Ca_2CuO_3 and Sr_2PdO_3 at maximum pressures. The diffracted X-rays were collected with an imaging plate. More details of the experimental setup are reported elsewhere.[30]

High resolution powder synchrotron XRD experiments under high pressures were performed at room temperature up to 37 GPa for Sr_2CuO_3, 51 GPa for Ca_2CuO_3, and 35 GPa for Sr_2PdO_3 using angle-dispersive X-ray diffractometry using the NE1A synchrotron beamline of the Photon Factory−Advanced Ring for Pulse X-rays (PF−AR) at the High Energy Accelerator Research Organization (KEK), Japan. Helium was used as a pressure transmitting medium for Sr_2CuO_3 and Sr_2PdO_3, while a 4:1 methanol/ethanol mixture was used for Ca_2CuO_3. The pressure gradients within the samples were not more

dx.doi.org/10.1021/ic201901a | *Inorg. Chem.* 2011, 50, 11787−11794

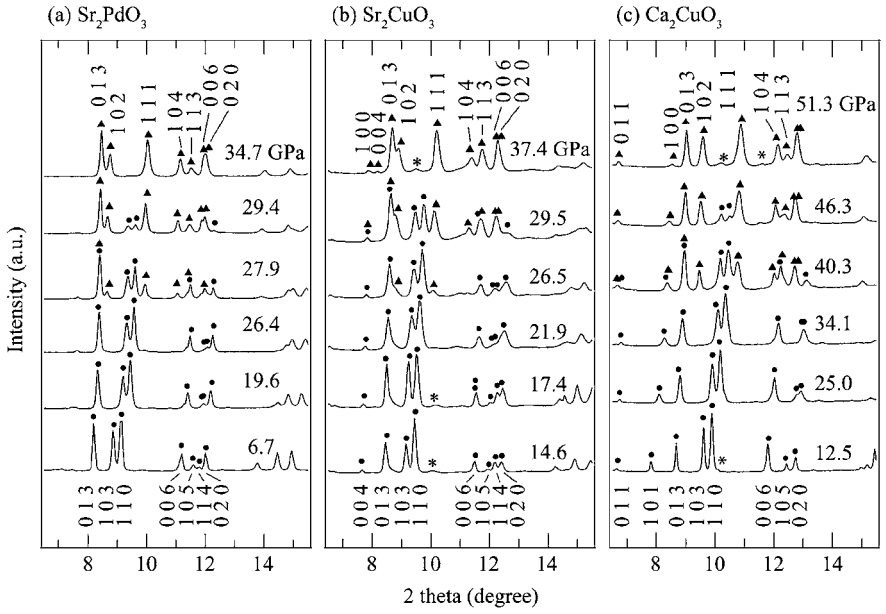

Figure 2. Selected powder synchrotron XRD patterns of (a) Sr_2PdO_3, (b) Sr_2CuO_3, and (c) Ca_2CuO_3 at room temperature under high pressures. For each specimen, the patterns can be indexed using the orthorhombic *I*-centered cell for $P < P_s$ and the orthorhombic *A*-centered cell for $P > P_s$. Peaks marked by circles and triangles, respectively, represent the low and high pressure phases. Peaks with asterisks denote unknown impurity.

than 8 GPa for Sr_2CuO_3, 4 GPa for Ca_2CuO_3, and 1 GPa for Sr_2PdO_3 at the maximum pressures applied in this study. The incident X-ray beam was monochromatized to a wavelength of 0.4115 Å for Sr_2CuO_3 and 0.4114 Å for Ca_2CuO_3. For Sr_2PdO_3, the first batch was measured with a wavelength of 0.4115 Å, until the used DAC was broken at 24 GPa. The second batch was measured with a wavelength of 0.4114 Å in a pressure range from 19 GPa to 35 GPa. The beam was collimated to a diameter of about 50 μm. The angle-dispersive XRD patterns were obtained on an imaging plate.

The observed synchrotron XRD intensities on the imaging plates were integrated as a function of 2θ using the Fit2d code[31] to obtain one-dimensional diffraction profiles. The data at the highest pressure applied to each compound were analyzed with the Rietveld method using the RIETAN-FP program.[32] The agreement indices used were the weighted pattern *R*, $R_{wp} = [\sum w_i(y_{io} - y_{ic})^2/\sum w_i(y_{io})^2]^{1/2}$; pattern *R*, $R_p = \sum|y_{io} - y_{ic}|/\sum(y_{io})$; and goodness of fit (GOF), $\chi^2 = [R_{wp}/R_{exp}]^2$, where $R_{exp} = [(N - m)/\sum w_i y_{io}{}^2]^{1/2}$. y_{io} and y_{ic} are the observed and calculated intensities, w_i is the weighting factor, *N* is the total number of y_{io} data when the background is refined, and *m* is the number of adjusted parameters.

Powder synchrotron XRD experiments for $LaSrNiO_{3.4}$ at pressures up to 70 GPa were performed at room temperature using angle-dispersive X-ray diffractometry using BL10XU of SPring-8. The powder sample was loaded into a 90 μm hole of preindented rhenium gaskets of the diamond anvil cells. A 4:1 methanol/ethanol mixture was used as a pressure transmitting medium. The Raman shift of diamond was used to determine the pressure.[33] The incident X-ray beam was monochromatized to a wavelength of 0.41417 Å. The beam was collimated to a diameter of about 30 μm.

The temperature dependence of the electric resistivity of Sr_2CuO_3 was carried out between 150 and 300 K using a standard four-probe DC resistance method at various constant pressures up to 40 GPa. Pt electrodes were used, and the sample/metal gasket cavity was coated with an insulating mixture of Al_2O_3 and NaCl combined with epoxy. Applied pressures were measured by means of a fluorescence manometer on ruby chips placed around the samples. In these electrical resistance measurements, the initial sectional area was about 60 μm × 50 μm, and the distance between probes was 50 μm.

3. RESULTS AND DISCUSSIONS

The high pressure synchrotron XRD measurements of Sr_2PdO_3, Sr_2CuO_3, and Ca_2CuO_3 at room temperature are summarized in Figures 5S−7S in the Supporting Information. Selected synchrotron XRD patterns are shown in Figure 2. Upon exclusion of weak unknown impurity peaks, the diffraction patterns of these compounds in the low pressure regime could be assigned to the orthorhombic *I*-centered unit cell, consistent with the reported data at ambient pressure.[27,28] As is expected, the 2θ angles of the reflection peaks gradually increase with increasing pressure, resulting from contraction of the lattice. For all of the compounds examined, the further application of pressure finally results in drastic change in the diffraction patterns featured by a discontinuous change in the cell constants and by modified reflection conditions compatible with the orthorhombic *A*-centered lattice. There is a pressure region where the low and high pressure phases coexist, mainly resulting from a pressure gradient across the specimen. We determined P_s as a pressure where the volume fractions of the two phases become close (Figure 8S in the Supporting Information). The obtained values are 29 GPa for Sr_2PdO_3, 30 GPa for Sr_2CuO_3, and 41 GPa for Ca_2CuO_3.

The cell constants of the Cu and Pd compounds, which are determined by the least-squares method using well-separated reflections in the synchrotron XRD profiles, are plotted as a function of pressure in Figure 3a−c. The pressure dependence of the volume below P_s (Figure 3d) can be fitted well by the Birch−Murnaghan equation of state.[34] The bulk modulus for Ca_2CuO_3, $K = 151 \pm 1$ GPa, is in a reasonable agreement with a previous study where $K = 165$ GPa.[35] Much smaller bulk moduli were obtained when the A site was strontium ($K = 99 \pm 3$ GPa for Sr_2CuO_3 and Sr_2PdO_3), suggesting that the compressibility is predominantly influenced by the A site. The number of ladder legs should not affect lattice compressibility because the low pressure phase of the two-legged ladder $Sr_3Fe_2O_5$ has a similar value of $K = 94$ GPa.[20]

dx.doi.org/10.1021/ic201901a | Inorg. Chem. 2011, 50, 11787−11794

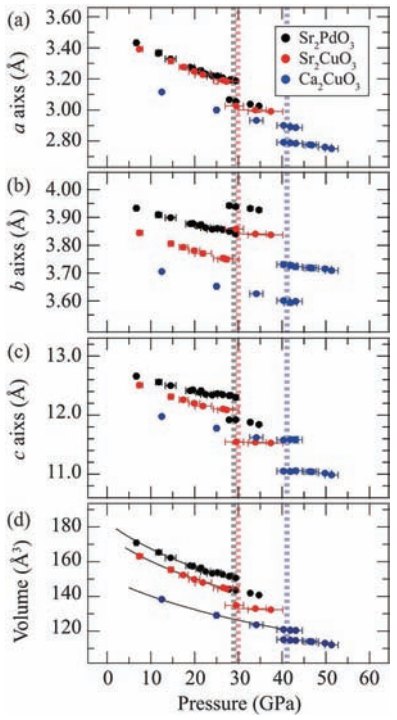

Figure 3. Pressure dependence of (a–c) the lattice parameters and (d) the volume for Sr_2CuO_3 (red), Sr_2PdO_3 (black), and Ca_2CuO_3 (blue). The parameters were obtained from synchrotron XRD measurements. Solid lines in d represent Birch–Murnaghan fitting for the low pressure phase below P_s.

Reflecting the topotactic nature of the structural transition, when the applied pressure is gradually reduced, the high pressure diffraction patterns completely returned to the low pressure diffraction patterns without any loss in crystallinity at 20.2 GPa for Sr_2PdO_3 and 29.7 GPa for Ca_2CuO_3 (see Figures 9S and 11S in the Supporting Information). Even when the pressure was quenched from the pressure above P_s, what we found was the original low pressure phase (Figure 6S in the Supporting Information). As shown in Figure 3a–c, the lattice evolution at P_s is anisotropic: The *a* and *c* axes exhibit a discontinuous decrease, while the *b* axis (i.e., the MO_2 chain direction) exhibits a discontinuous increase. This is indeed what has been observed in $Sr_3Fe_2O_5$.[20] The change in the *a* and *b* axes at P_s is about −4% and +2% for Sr_2PdO_3 and −4% and +3% for Sr_2CuO_3 and Ca_2CuO_3, which are comparable to −3% and +2% for $Sr_3Fe_2O_5$.[20] All of these observations suggest that the structural transitions in Sr_2PdO_3, Sr_2CuO_3, and Ca_2CuO_3 are analogous to that in $Sr_3Fe_2O_5$. Namely, the structural transition is described by a phase shift of the neighboring MO_2 chains from (1/2,1/2,1/2) to (0,1/2,1/2), which allows a change in the A-site coordination environment from the *B*1-type to *B*2-type geometry (Figure 1a and b).

The laboratory XRD data could also be assigned as the orthorhombic *I*-centered lattice for $P < P_s$ and the orthorhombic *A*-centered lattice for $P_s < P$ (Figures 9S–11S in the Supporting Information). Although there are only three reflections available for the calculation ((013), (103), and (110) for the low pressure phase and (013), (102), and (111) for the high pressure phase), the pressure dependence of the lattice parameters for the low and high pressure phases and the bulk moduli for the low pressure phase (K = 152 ± 1 GPa for Ca_2CuO_3, K = 98 ± 4 GPa for Sr_2CuO_3, and K = 94 ± 4 GPa for Sr_2PdO_3) agree nicely with those of the synchrotron XRD data (Figure 12S in the Supporting Information). However, precise determination of P_s and lattice paramters in the vicinity of P_s was rather difficult. Discontinuous changes of the lattice parameteres at P_s (as observed from the synchrotron XRD data) were less obvious, and there is a slight deviation of P_s (<7 GPa) between those estimated from synchrotron XRD and laboratory XRD experiments.

There are several reasons that hamper precise determination of lattice parameters and critical pressure from the laboratory XRD data. First, at pressures close to P_s, the low and high pressure phases coexist because of the pressure gradient, and the three peaks available for identifying each phase overlap with each other due to the low resolution of the instrument. Second, the beam size for the laboratory XRD experiments is much larger than for the synchrotron XRD experiments and is comparable with the size of the specimen, resulting in a larger pressure gradient. Third, in the Sr_2PdO_3 experiment, a methanol/ethanol mixture was used as a pressure transmitting medium, which should cause nonhydrostatic stress when compared with helium. Note that, in both the synchrotron and laboratory XRD experiments for Ca_2CuO_3, we used a methanol/ethanol mixture as a pressure transmitting medium. This is because the experiments for Ca_2CuO_3 require a higher pressure, and helium often cause breakage of a diamond culet.

The high pressure A_2MO_3 structure was refined using the synchrotron XRD data at 34.7 GPa for Sr_2PdO_3, at 37.4 GPa for Sr_2CuO_3, and at 51.3 GPa for Ca_2CuO_3, assuming the space group *Ammm* (as in $Sr_3Fe_2O_5$[20]). The atoms are placed at 4*j* (0.5, 0, *z*) for A = Sr or Ca, 2*a* (0, 0, 0) for M = Cu or Pd, 4*i* (0, 0, *z*) for O(1), and 2*b* (0, 0.5, 0) for O(2). During the refinements, the occupancy factors were constrained to unity. All of the refinements converged well, yielding R_p = 0.75%, R_{wp} = 1.21%, χ^2 = 2.83 R_{Bragg} = 0.97%, and R_F = 0.46% for Sr_2PdO_3; R_p = 0.90%, R_{wp} = 1.20%, χ^2 = 2.49, R_{Bragg} = 0.57%, and R_F = 0.31% for Sr_2CuO_3; and R_p = 0.69%, R_{wp} = 1.24%, χ^2 = 1.59, R_{Bragg} = 1.08%, and R_F = 0.49% for Ca_2CuO_3 (Figure 4). The atomic displacement parameters *B* for each atom are acceptable. The final structural parameters together with reliability factors based on the *Ammm* space group are summarized in Table 1. We note that other lower symmetry space groups which satisfy the reflection conditions for the high pressure phase (i.e., *A*2*mm*, *Am*2*m*, *Amm*2, and *A*222) did not improve the structural refinements.

The interatomic distances for the refined structures are listed in Table 2. The A-site ions in the low pressure phase are coordinated to seven oxygen atoms (A–O(1) × 1, A–O(1) × 4, A–O(2) × 2) in the *B*1-type arrangement (Figure 1a), while in the high pressure phase they are coordinated to eight oxygen atoms (where A–O(1) × 1 → A–O(1) × 2) in the *B*2-type arrangement (Figure 1b). The A–O distances (2.226–2.564 Å) for the high pressure phase are acceptable considering known compounds in this pressure region.[10,19,20,36–38] The Cu–O distances (1.84–2.016 Å) for the high pressure phases are also comparable to those found in previous studies.[39,40]

Now that the proposed high pressure structure of A_2MO_3 is confirmed, we can say that the pressure-induced *B*1-to-*B*2 transition generally occurs in the rock salt/spin-ladder intergrowth compounds and is not restricted to iron oxides and/or a two-legged ladder structure. Namely, we can propose that $(AO)(AMO_2)_n$ (n = 1, 2, 3, etc.) with the AO rock salt unit and the $(AMO_2)_n$ *n*-legged spin ladder unit, if synthesized, would exhibit the same type of transition. It also gives proof

dx.doi.org/10.1021/ic201901a | *Inorg. Chem.* 2011, 50, 11787–11794

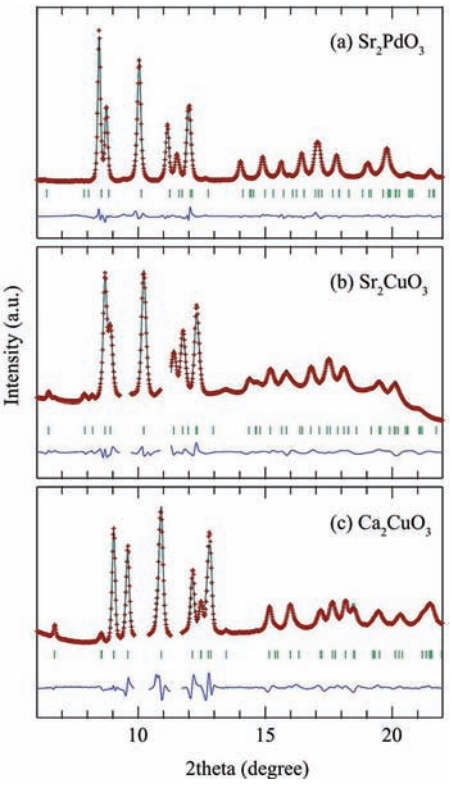

Figure 4. Observed (crosses), calculated (lines), and difference plots from the structural refinements of the powder synchrotron XRD data for (a) Sr_2PdO_3 at 34.7 GPa, (b) Sr_2CuO_3 at 37.4 GPa, and (c) Ca_2CuO_3 at 51.3 GPa. The ticks represent the positions of the calculated Bragg reflections. Ranges for 9.3−9.7° and 10.9−11.3° in b and 9.8−10.4° and 11.3−11.7° in c are excluded from the refinement because of the existence of unknown impurities.

Table 1. Rietveld Refinement for A_2MO_3 (A = Sr, Ca; M = Cu, Pd)[a]

	Sr_2PdO_3 at 34.7 GPa	Sr_2CuO_3 at 37.4 GPa	Ca_2CuO_3 at 51.3 GPa
a (Å)	3.0277(2)	2.9859(3)	2.7496(3)
b (Å)	3.9293(3)	3.8445(7)	3.7044(5)
c (Å)	11.8447(9)	11.497(2)	11.029(1)
z for A	0.6570(2)	0.6589(2)	0.6587(4)
z for O(1)	0.8298(8)	0.840(2)	0.830(1)
B for A (Å^2)	0.14(8)	1.3(1)	0.2(2)
B for M (Å^2)	0.31(7)	2.3(1)	0.3(2)
B for O(1) and O(2) (Å^2)	0.2(2)	1.8(2)	0.5(2)
R_{wp} (%)	1.21%	1.20%	1.24%
R_p (%)	0.75%	0.90%	0.69%
χ^2	2.83	2.49	1.59
R_{Bragg} (%)	0.97%	0.57%	1.08%
R_F (%)	0.46%	0.31%	0.49%

[a]All of the refinements were performed using the *Ammm* space group with A on 4*j* (0.5, 0, *z*), M on 2*a* (0, 0, 0), O(1) on 4*i* (0, 0, *z*), and O(2) on 2*b* (0, 0.5, 0).

that the structural transition in $Sr_3Fe_2O_5$ at 30 GPa is independent of other magnetic/transport transitions at 34 GPa.

We may further expect that the *B*1-to-*B*2 transition is more general and is observed for intergrowth structures having a rock salt sublayer. Among possible candidates are K_2NiO_2[41] and A_2ZnN_2 (A = Sr, Ba),[42] the structures of which differ from the A_2MO_3 structure by the absence of bridging oxygen (thus *I*4/*mmm*), yielding a 2-fold dumbbell coordination around Ni and Zn. The structure of Ba_3ZnN_2O is built up from the intergrowth structure between the BaO rock salt block and Ba_2ZnN_2 block.[43] Misfit layer compounds $(MS)_nTS_2$ (M = Sn, Pb, Bi, rare earth elements; T = Nb, Ta; n = 1.08−1.19) are intergrowth structures between distorted MS rock salt blocks and TS_2 blocks.[44] Delafossite $CuFeO_2$ consists of an FeO rock salt block and linearly coordinated CuO block. Xu et al. reported the high pressure transition leading to an increase of Cu coordination at 23 GPa,[39] instead of a *B*1-to-*B*2 transition in the FeO block. Further high pressure possibly leads to the *B*1-to-*B*2 transition.

Let us now quantitatively compare the *B*1-to-*B*2 structural transition between binary systems and the intergrowth systems. It is known from experimental and theoretical studies in binary oxides or chalcogenides (AX) that for a given X, log P_s follows a linear pressure dependence on R_A/R_X (Figure 1S in the Supporting Information).[6−8,45] Figure 5 shows the empirical relation for X = oxygen, where log $P_s = -2.0(R_A/R_O) + 3.2$. It is remarkable that the critical pressures for the intergrowth compounds A_2MO_3 and $Sr_3Fe_2O_5$ are located just on the line. This means that P_s is determined solely by R_A/R_O in the AO block. Insensitivity of the ladder block to P_s in turn implies that the ladder subunit at ambient pressure is a favorable form at high pressure. The structural stability of the ladder subunit under high pressure is understandable because it should have high compressibility along the out-of-plane direction as a result of the complete absence of apical oxygen. In support of this, a preliminary experiment showed that the infinite layer structure $SrFeO_2$ consisting only of the infinite-legged ladder block does not show any structural transition at least up to 100 GPa. As shown in Figure 13S (Supporting Information), the *a* axis and *b* axes of A_2MO_3 and $Sr_3Fe_2O_5$ show nearly the same pressure dependences as the *c* and *a* axes of $SrFeO_2$, implying that the ladder subunit is already structurally optimized.

When the vacant apical oxygen site of the MO_4 square plane is partially filled, does this type of structural transition occur, and if it does, how and to what extent is P_s influenced? To answer these questions, we performed a high pressure synchrotron XRD measurement on $LaSrNiO_{3.4}$. Here, $LaSrNiO_3$ without apical oxygen is isostructural with Sr_2CuO_3. At ambient pressure, $LaSrNiO_{3.4}$ adopts the orthorhombic *I*-centered space group, sharing the same structural feature with Sr_2CuO_3 but differing in that the apical oxygen site at 2*d* (0.5, 0, 0) is partially (i.e., 40%) and randomly occupied (Figure 14Sa, Supporting Information). The ratio R_A/R_O in $LaSrNiO_{3.4}$ is 0.86 (R_A is the average ionic radius of La^{3+} and Sr^{2+}). Then, P_s is estimated as 30 GPa on the basis of the P_s-R_A/R_O line in Figure 5. However, the synchrotron XRD patterns of $LaSrNiO_{3.4}$ at 44 and 55 GPa shown in Figure 6 could still be assigned to the *I*-centered orthorhombic unit cell. A set of new peaks assigned to the *A*-centered orthorhombic unit cell emerged at 63 GPa together with those of the original *I*-centered unit cell. The 70 GPa profile indicates the completion of the structural transition. Since the strongest reflections, (110) for the low pressure phase and (111) for the high pressure phase, are of comparable intensity at 63 GPa, P_s should be around this pressure. The lattice parameters at 55 and 70 GPa are, respectively, a = 3.401(2) Å, b = 3.637(2) Å, and c = 11.99(2) Å and a = 3.124(2) Å, b = 3.727(2) Å, and c = 10.568(7) Å. The increased *b* axis, a characteristic feature of the *B*1-to-*B*2 transition, is observed. In addition, as a consequence

dx.doi.org/10.1021/ic201901a | *Inorg. Chem.* 2011, 50, 11787−11794

Table 2. Interatomic Distances and Ratios between M−O(1) and M−O(2) for A_2MO_3 (A = Sr, Ca; M = Cu, Pd)

	Sr_2PdO_3		Sr_2CuO_3		Ca_2CuO_3	
bond (Å)	0 GPa[18]	34.7 GPa	0 GPa[16]	37.4 GPa	0 GPa[16]	51.3 GPa
A−O(1) × 1	2.467		2.510		2.289	
A−O(1) × 2		2.3982(14)		2.360(2)		2.226(3)
A−O(1) × 4	2.671	2.545(8)	2.629	2.4339(3)	2.490	2.3103(7)
A−O(2) × 2	2.588	2.4851(6)	2.570	2.564(15)	2.466	2.332(9)
M−O(1) × 2	2.068	2.016(9)	1.967	1.84(2)	1.959	1.880(11)
M−O(2) × 2	1.993	1.9646(2)	1.958	1.9223(3)	1.884	1.8522(3)
			ratio			
M−O(1)/M−O(2)	1.038	1.026	1.005	0.957	1.040	1.015

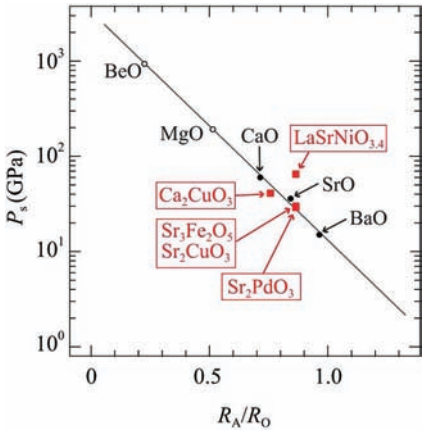

Figure 5. P_s vs the A-site ion radius (R_A) to the oxide ion radius (R_O). R_A in 6-, 7-, and 8-fold coordination is used,[45] respectively, for the low pressure structure of AO, A_2MO_3 ($Sr_3Fe_2O_5$), and $LaSrNiO_{3.4}$. Experimental (black closed circles) and theoretical (black open circles) values for binary systems AO (A = Ca, Sr, Ba) are from the refs 9−11. Red closed squares represent the data obtained in this study.

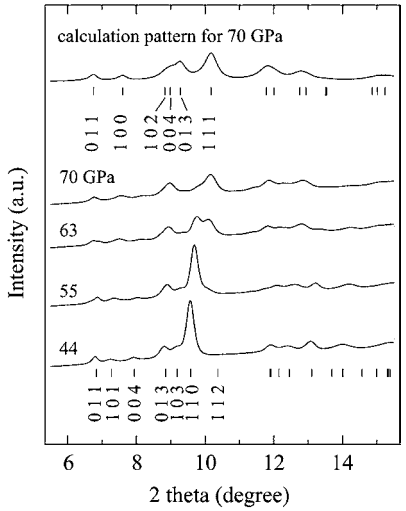

Figure 6. Powder synchrotron XRD patterns of $LaSrNiO_{3.4}$ under high pressures collected at room temperature. The data at 44 GPa were indexed by the *I*-centered orthorhombic unit cell, while those at 70 GPa were indexed by the *A*-centered orthorhombic unit cell. The ticks represent the positions of the allowed Bragg reflections. The calculation pattern for 70 GPa is obtained from the expected high pressure structure as shown in Table 1S in the Supporting Information.

of the partial occupation at the apical vacant site, the distance between the face-to-face square planes (*a* axis) is considerably longer as compared with those of other compounds, e.g., 2.7496(3) Å (= *a*) for Ca_2CuO_3 at 51.3 GPa and 2.947 Å (= *c*) for $SrFeO_2$ at 70.4 GPa (unpublished data).

$P_s \sim 63$ GPa for $LaSrNiO_{3.4}$ is twice as high as that estimated from the empirical relation for the binary rock salt systems and for the rock salt/ladder intergrowth compounds (see Figure 5). Obviously, P_s is affected by the partial occupancy at the apical site. Given the less efficient contraction of the *a* axis in the pressure study of $LaSrNiO_{3.4}$, it is naturally considered that P_s depends on the amount of apical oxygen in $LaSrNiO_{3+x}$; the more the apical oxygen atoms there are, the higher P_s becomes. Ultimately, the fully occupied compound $LaSrNiO_4$ ($x = 1$; K_2NiO_4-type structure), or in more general terms, Ruddlesden−Popper phase $A_{n+1}B_nO_{3n+1}$ ($n = 1, 2, 3$, etc.), should undergo the same type of structural transition at elevated pressures. A simple linear extrapolation of the critical pressures (63 GPa for $LaSrNiO_{3.4}$ and 30 GPa for $LaSrNiO_3$) gives $P_s \sim$ 120 GPa for $LaSrNiO_4$—a pressure range at which synchrotron XRD experiments are currently accessible.[4]

Ruddlesden−Popper-type layered perovskite compounds have offered a wide range of chemical and physical properties, including superconductivity in $(La,Sr)CuO_4$ and Sr_2RuO_4,[46,47] colossal magnetoresistivity (CMR) in $(La,Sr)_{n+1}Mn_nO_{3n+1}$,[48] itinerant ferromagnetism in $Sr_3Ru_2O_7$,[49] Mott insulating behavior derived from the strong spin−orbit coupling in Sr_2IrO_4,[50] and photocatalysis in Sr_2TiO_4. As far as the authors are aware, this type of structural transition has not been reported yet. Thus, it is very interesting to investigate if the structural transition occurs generally in Ruddlesden−Popper compounds or not. It is expected that the phase change of adjacent perovskite blocks can change the electronic structures, leading to new or improved chemical and physical properties.

The ambient pressure phase of Sr_2CuO_3 is well-known as a prototypical 1D spin-1/2 Heisenberg antiferromagnet with $T_N/J_{intra} \sim 0.002$ (where J_{inta} is the intrachain superexchange interaction).[51,52] The staggered arrangement of the adjacent CuO_2 chains renders the Cu $d_{x^2-y^2}$ orbitals to be only weakly overlapped between the chains, strongly enhancing the one-dimensionality of the magnetic interactions. Upon the structural transition, the adjacent chains align in a uniform manner to form a $(CuO_3)^{4-}$ "quasi" infinite layer structure. As a result, the interchain interaction via a Cu−O−O−Cu super-super-exchange interaction path within each $(CuO_3)^{4-}$ layer would not be negligible, making the system a quasi 2D antiferromagnet.

In order to detect a sign of possible effects from an increase in dimensionality, we investigated the transport properties of

dx.doi.org/10.1021/ic201901a | Inorg. Chem. 2011, 50, 11787−11794

Sr_2CuO_3 at elevated pressure. Shown in Figure 7 is the pressure dependence of room-temperature resistance ρ(RT) of

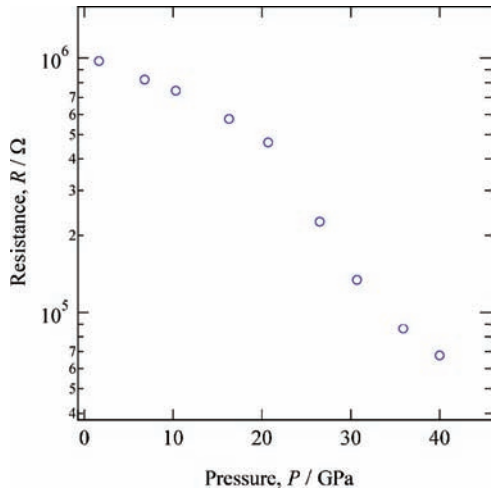

Figure 7. Room-temperature electrical resistance of Sr_2CuO_3 as a function of *P*.

Sr_2CuO_3. Reflecting a wide band gap (~2 eV) in the ambient pressure structure,[53,54] ρ(RT) at 2 GPa is about 10^6 Ω (roughly corresponding to 10^3 to 10^4 Ωcm). ρ(RT) decreases slowly toward ~20 GPa and then decreases rather steeply above P_s, an indication of a reduced band gap and/or an increased electron mobility/carrier number in the high pressure phase. The anomaly associated with the structural transition is not so obvious, which is understood in terms of a large pressure distribution along the sample and the use of hand-pressed pellet, as was seen in $SrFeO_2$ and $Sr_3Fe_2O_5$.[19,20] A crude estimation of the activation energy, as calculated from temperature dependence of the resistances, gave ~0.21 eV below P_s and ~0.18 eV above P_s (Figures 15S and 16S in the Supporting Information). We would like to recall that in the two-legged ladder structure $(Sr,Ca)_{14}Cu_{24}O_{41}$, pressure induces dimensional crossover from 1D to 2D as well as charge-transfer from the chain to the ladder, and as a consequence superconductivity appears.[55] At present, it is not clear yet if the reduced band gap in Sr_2CuO_3 above P_s is explained by the dimensional increase from 1D to 2D. Carrier doping into the $(CuO_3)^{4-}$ layer, for example, by Na-for-Sr substitution may eventually induce metallic conductivity. Because of experimental limits at high pressure, first principles calculations would be definitely useful for understanding the electronic structures and the nature of the chemical bonds between the magnetic moments.

4. CONCLUSION

We have demonstrated that the intergrowth structures A_2MO_3 (A = Sr, Ca; M = Cu, Pd) exhibit a pressure-induced structural transition with the space group changing from *Immm* to *Ammm*, involving a change of the structure of AO block from the rock salt structure to a CsCl structure. Together with $Sr_3Fe_2O_5$, the present study demonstrates the generality of the *B*1-to-*B*2 structural transition in the intergrowth structure of $(AO)(AMO_2)_n$ (n = 1, 2, 3, etc.). It is remarkable that the critical pressures P_s for the intergrowth compounds are determined solely by R_A/R_O, showing quantitatively the same trend as the binary AO compounds, which make it possible to predict the P_s of other related compounds. Given the *B*1-to-*B*2 structural transition in binary chalcogenides,[6−18] the rock-salt/ladder intergrowth chalcogenides may also exhibit the *B*1-to-*B*2 structural transition with P_s scaled by R_A/R_S, R_A/R_{Se}, and R_A/R_{Te}. The introduction of an oxygen atom at the apical site leads to a significant deviation from the P_s vs R_A/R_O relation. It is expected that the high pressure structures consisting of "quasi" infinite layers have different electronic structures due to interladder(chain) interaction within the layer, leading to new or improved chemical and physical properties. Unfortunately, we have not successfully quenched the high pressure phase, which is an important step for investigating detailed properties and future applications. Recently, the high pressure *B*2 structure of the KI crystal was obtained even at ambient pressure using nanospaces of single-walled carbon nanohorns.[56] Thus, novel techniques may be necessary and hold the key for tapping into high pressure materials for widespread use.

■ ASSOCIATED CONTENT

Ⓢ Supporting Information

Experimental details and characterization data for the new compounds. This material is available free of charge via the Internet at http://pubs.acs.org.

■ AUTHOR INFORMATION

Corresponding Author

*E-mail: kage@scl.kyoto-u.ac.jp.

■ ACKNOWLEDGMENTS

This work was supported by the Japan Society for the Promotion of Science (JSPS) through its "Funding Program for World-Leading Innovative R&D on Science and Technology (FIRST) Program"; by Grants-in-Aid for Science Research in the Priority Area "Novel States of Matter Induced by Frustration" (No. 19052004); by a Grant-in-Aid for Scientific Research (A) (No. 22245009) from the Ministry of Education, Culture, Sports, Science and Technology of Japan; and by the Global COE program International Center Science, Kyoto University, Japan. Synchrotron beam time at BL10XU of SPring-8 was supported by "Priority Program for Disaster-Affected Quantum Beam Facilities" (2010G560 for KEK and 2011A1944 for SPring-8). T.Y. was supported by the Japan Society for the Promotion of Science for Young Scientists. T.K. acknowledges partial support from the Foundation "Hattori-Hokokai" and "Strategic Research Base Development" Program for Private Universities subsidized by MEXT (2009, S0901022).

■ REFERENCES

(1) Park, K. T.; Terakura, K.; Matsui, Y. *Nature* **1988**, *336*, 670−672.
(2) Andrault, D.; Fiquet, G.; Guyot, F.; Hanfland, M. *Science* **1998**, *282*, 720−724.
(3) Teter, D. M.; Hemley, R. J.; Kresse, G.; Hafner, J. *Phys. Rev. Lett.* **1998**, *80*, 2145−2148.
(4) Kuwayama, Y.; Hirose, K.; Sata, N.; Ohishi, Y. *Science* **2005**, *309*, 923−925.
(5) Murakami, M.; Hirose, K.; Kawamura, K.; Sata, N.; Ohishi, Y. *Science* **2004**, *304*, 855−858.
(6) Syassen, K. *Phys. Status Solidi* **1985**, *91*, 11−15.
(7) Ekbundit, S.; Chizmeshya, A.; LaViolette, R.; Wolf, G. H. *J. Phys.: Condens. Matter.* **1996**, *8*, 8251−8265.
(8) Narayana, C.; Nesamony, V. J.; Ruoff, A. L. *Phys. Rev. B* **1997**, *56*, 14338−14343.
(9) Liu, L.; Bassett, W. A. *J. Geophys. Res.* **1972**, *77*, 4934−4937.

(10) Jeanloz, R.; Ahrens, T. J.; Mao, H. K.; Bell, P. M. *Science* **1979**, *206*, 829−830.
(11) Sato, Y.; Jeanloz, R. *J. Geophys. Res.* **1981**, *86*, 11773−11778.
(12) Grzybowski, T. A.; Ruoff, A. L. *Phys. Rev. B* **1983**, *27*, 6502−6503.
(13) Grzybowski, T. A.; Ruoff, A. L. *Phys. Rev. Lett.* **1984**, *53*, 489−492.
(14) Zimmer, H. G.; Winzen, H.; Syassen, K. *Phys. Rev. B* **1985**, *32*, 4066−4070.
(15) Grzybowski, T. A.; Ruoff, A. L. *Mater. Res. Soc. Symp. Proc.* **1984**, 43−47.
(16) Weir, S. T.; Vohra, Y. K.; Ruoff, A. L. *Phys. Rev. B* **1986**, *33*, 4221−4226.
(17) Luo, H.; Greene, R. G.; Ruoff, A. L. *Phys. Rev. B* **1994**, *49*, 15341−15343.
(18) Luo, H.; Greene, R. G.; Ghandehari, K.; Li, T.; Ruoff, A. L. *Phys. Rev. B* **1994**, *50*, 16232−16237.
(19) Kawakami, T.; Tsujimoto, Y.; Kageyama, H.; Chen, X. Q.; Fu, C. L.; Tassel, C.; Kitada, A.; Suto, S.; Hirama, K.; Sekiya, Y.; Makino, Y.; Okada, T.; Yagi, T.; Hayashi, N.; Yoshimura, K.; Nasu, S.; Podloucky, R.; Takano, M. *Nature Chem.* **2009**, *1*, 371−376.
(20) Yamamoto, T.; Tassel, C.; Kobayashi, Y.; Kawakami, T.; Okada, T.; Yagi, T.; Yoshida, H.; Kamatani, T.; Watanabe, Y.; Kikegawa, T.; Takano, M.; Yoshimura, K.; Kageyama, H. *J. Am. Chem. Soc.* **2011**, *133*, 6036−6043.
(21) Takano, M.; Takeda, Y.; Okada, H.; Miyamoto, M.; Kusaka, T. *Physica C* **1989**, *159*, 375−378.
(22) Hiroi, Z.; Azuma, M.; Takano, M.; Bando, Y. *J. Solid State Chem.* **1991**, *95*, 230−238.
(23) Pruneda, J. M.; Íñiguez, J.; Canadell, E.; Kageyama, H.; Takano, M. *Phys. Rev. B* **2008**, *78*, 115101.
(24) Xiang, H. J.; Wei, S. H.; Whangbo, M. H. *Phys. Rev. Lett.* **2008**, *100*, 167207.
(25) Koo, H. J.; Xiang, H.; Lee, C.; Whangbo, M. H. *Inorg. Chem.* **2009**, *48*, 9051−9053.
(26) Tomiyasu, K.; Kageyama, H.; Lee, C.; Whangbo, M. H.; Tsujimoto, Y.; Yoshimura, K.; Taylor, J. W.; Llobet, A.; Trouw, F.; Kakurai, K.; Yamada, K. *J. Phys. Soc. Jpn.* **2010**, *79*, 034707.
(27) Weller, M. T.; Lines, D. R. *J. Solid State Chem.* **1989**, *82*, 21−29.
(28) Nagata, Y.; Taniguchi, T.; Tanaka, G.; Satho, M.; Samata, H. *J. Alloys Compd.* **2002**, *346*, 50−56.
(29) Crespin, M.; Landron, C.; Odier, P.; Bassat, J. M.; Mouron, P.; Choisnet, J. *J. Solid State Chem.* **1992**, *100*, 281−291.
(30) Arora, A. K.; Yagi, T.; Miyajima, N.; Mary, T. A. *J. Appl. Phys.* **2005**, *97*, 013508.
(31) Hammersley, J. *Fit2d User Manual*; ESRF: Grenoble, France, 1996.
(32) Izumi, F.; Momma, K. *Solid State Phenom.* **2007**, *130*, 15−20.
(33) Akahama, Y.; Kawamura, H. *J. Appl. Phys.* **2004**, *96*, 3748−3751.
(34) Birch, F. *J. Appl. Phys.* **1938**, *9*, 279−288.
(35) Zhang, G. M.; Mai, W. J.; Li, F. Y.; Bao, Z. X.; Yu, R. C.; Lu, T. Q.; Liu, J.; Jin, C. Q. *Phys. Rev. B* **2003**, *67*, 212102.
(36) Errandonea, D.; Pellicer-Porres, J.; Manjón, F. J.; Segura, A.; Ferrer-Roca, C.; Kumar, R. S.; Tschauner, O.; Rodríguez-Hernández, P.; López-Solano, J.; Radescu, S.; Mujica, A.; Muñoz, A.; Aquilanti, G. *Phys. Rev. B* **2005**, *72*, 174106.
(37) Errandonea, D.; Kumar, R. S.; Ma, X.; Tu, C. *J. Solid State Chem.* **2008**, *181*, 355−364.
(38) Fischer, M.; Bonello, B.; Itie, J. P.; Polian, A.; Dartyge, E.; Fontaine, A.; Tolentino, H. *Phys. Rev. B* **1990**, *42*, 8494−8498.
(39) Xu, W. M.; Rozenberg, G. K.; Pasternak, M. P.; Kertzer, M.; Kurnosov, A.; Dubrovinsky, L. S.; Pascarelli, S.; Munoz, M.; Vaccari, M.; Hanfland, M.; Jeanloz, R. *Phys. Rev. B* **2010**, *81*, 104110.
(40) Dera, P.; Jayaraman, A.; Prewitt, C. T.; Gramsch, S. A. *Phys. Rev. B* **2002**, *65*, 134105.
(41) Rieck, H.; Hoppe, R. *Z. Anorg. Allg. Chem.* **1973**, *400*, 311−320.
(42) Yamane, H.; DiSalvo, F. J. *J. Solid State Chem.* **1995**, *119*, 375−379.
(43) Yamane, H.; DiSalvo, F. J. *J. Alloys Compd.* **1996**, *234*, 203−206.
(44) Wiegers, G. A.; Meetsma, A.; Van Smaalen, S.; Haange, R. J.; Wulff, J.; Zeinstra, T.; De Boer, J. L.; Kuypers, S.; Van Tendeloo, G.; Van Landuyt, J.; Amelinckx, S.; Meersehaut, A.; Rabu, P.; Rouxel, J. *Solid State Commun.* **1989**, *70*, 409−413.
(45) Shannon, R. *Acta Crystallogr.* **1976**, *32*, 751−767.
(46) Cava, R. J.; Van Dover, R. B.; Batlogg, B.; Rietman, E. A. *Phys. Rev. Lett.* **1987**, *58*, 408−410.
(47) Maeno, Y.; Hashimoto, H.; Yoshida, K.; Nishizaki, S.; Fujita, T.; Bednorz, J. G.; Lichtenberg, F. *Nature* **1994**, *372*, 532−534.
(48) Moritomo, Y.; Asamitsu, A.; Kuwahara, H.; Tokura, Y. *Nature* **1996**, *380*, 141−144.
(49) Cao, G.; McCall, S.; Crow, J. E. *Phys. Rev. B* **1997**, *55*, 672−675.
(50) Kim, B. J.; Ohsumi, H.; Komesu, T.; Sakai, S.; Morita, T.; Takagi, H.; Arima, T. *Science* **2009**, *323*, 1329−1332.
(51) Motoyama, N.; Eisaki, H.; Uchida, S. *Phys. Rev. Lett.* **1996**, *76*, 3212−3215.
(52) Takigawa, M.; Motoyama, N.; Eisaki, H.; Uchida, S. *Phys. Rev. Lett.* **1996**, *76*, 4612−4615.
(53) Mackrodt, W. C.; Gotsis, H. J. *Phys. Rev. B* **2000**, *62*, 10728−10736.
(54) Suzuura, H.; Yasuhara, H.; Furusaki, A.; Nagaosa, N.; Tokura, Y. *Phys. Rev. Lett.* **1996**, *76*, 2579−2582.
(55) Nagata, T.; Uehara, M.; Goto, J.; Akimitsu, J.; Motoyama, N.; Eisaki, H.; Uchida, S.; Takahashi, H.; Nakanishi, T.; Môri, N. *Phys. Rev. Lett.* **1998**, *81*, 1090−1093.
(56) Urita, K.; Shiga, Y.; Fujimori, T.; Iiyama, T.; Hattori, Y.; Kanoh, H.; Ohba, T.; Tanaka, H.; Yudasaka, M.; Iijima, S.; Moriguchi, I.; Okino, F.; Endo, M.; Kaneko, K. *J. Am. Chem. Soc.* **2011**, *133*, 10344−10347.